
Mapping Arginase Expression with ^{18}F -Fluorinated Late-Generation Arginase Inhibitors Derived from Quaternary α -Amino Acids

Gonçalo S. Clemente¹, Inês F. Antunes¹, Santosh Kurhade², Mariska P.M. van den Berg³, Jürgen W.A. Sijbesma¹, Aren van Waarde¹, Rogier C. Buijsman⁴, Nicole Willemsen-Seegers⁴, Reinoud Gosens³, Herman Meurs³, Alexander Dömling², and Philip H. Elsinga¹

¹Department of Nuclear Medicine and Molecular Imaging, University Medical Center Groningen, University of Groningen, Groningen, The Netherlands; ²Department of Drug Design, University of Groningen, Groningen, The Netherlands; ³Department of Molecular Pharmacology, University of Groningen, Groningen, The Netherlands; and ⁴Netherlands Translational Research Center B.V., Oss, The Netherlands

Arginase hydrolyzes L-arginine and influences levels of polyamines and nitric oxide. Arginase overexpression is associated with inflammation and tumorigenesis. Thus, radiolabeled arginase inhibitors may be suitable PET tracers for staging arginase-related pathophysiologies. We report the synthesis and evaluation of 2 radiolabeled arginase inhibitors, ^{18}F -FMARS and ^{18}F -FBMARS, developed from α -substituted-2-amino-6-boronohexanoic acid derivatives. **Methods:** Arylboronic ester-derived precursors were radiolabeled via copper-mediated fluorodeboronation. Binding assays using arginase-expressing PC3 and LNCaP cells were performed. Autoradiography of lung sections from a guinea pig model of asthma overexpressing arginase and dynamic small-animal PET imaging with PC3-xenografted mice evaluated the radiotracers' specific binding and pharmacokinetics. **Results:** ^{18}F -fluorinated compounds were obtained with radiochemical yields of up to 5% (decay-corrected) and an average molar activity of $53 \text{ GBq} \cdot \mu\text{mol}^{-1}$. Cell and lung section experiments indicated specific binding that was blocked up to 75% after pretreatment with arginase inhibitors. Small-animal PET studies indicated fast clearance of the radiotracers ($7.3 \pm 0.6 \text{ min}$), arginase-mediated uptake, and a selective tumor accumulation (SUV, 3.0 ± 0.7). **Conclusion:** The new ^{18}F -fluorinated arginase inhibitors have the potential to map increased arginase expression related to inflammatory and tumorigenic processes. ^{18}F -FBMARS showed the highest arginase-mediated uptake in PET imaging and a significant difference between uptake in control and arginase-inhibited PC3 xenografted mice. These results encourage further research to examine the suitability of ^{18}F -FBMARS for selecting patients for treatments with arginase inhibitors.

Key Words: ^{18}F ; arginase; arginase inhibitors; PET

J Nucl Med 2021; 62:1163–1170

DOI: 10.2967/jnumed.120.255968

Arginase is a manganese-dependent metalloenzyme that catalyzes the hydrolysis of L-arginine to L-ornithine and urea. Cytosolic arginase type I (Arg1) is expressed predominantly in the liver and

involved in ureagenesis, whereas mitochondrial type II (Arg2) is expressed throughout extrahepatic tissues (1). Arginase levels inversely influence the activity of endothelial, neuronal, and inducible nitric oxide synthases (NOSs), a group of enzymes competing for the same substrate (L-arginine) to catalyze the production of nitric oxide (NO^{\bullet}). This highly diffusive and reactive gas is important in cell signaling to induce, for example, relaxation of airway and vascular smooth muscle, neurotransmission, and regulation of the immune system (2). The delicate arginase–NOS physiologic equilibrium can be disrupted by oxidative and inflammatory signaling pathways (Fig. 1) (2,3).

Arginase overexpression, and the consequent reduction of NO^{\bullet} and increase of proline and polyamines levels, have been associated with a series of pathologies that range from cardiovascular, immune-mediated, and inflammatory conditions to mental disorders (2). Additionally, arginase is upregulated by myeloid cells in several tumor microenvironments at very early stages, being associated with poor outcomes (4). Moreover, tumor cells typically overexpress arginase to promote cell proliferation and evade the immune system (5). Thus, arginase is a potential therapeutic target, and potent arginase inhibitors were developed (2,6–8).

Some of the most potent arginase inhibitors reported in the literature were developed and patented by Mars, Inc. (9,10). The presence of a chlorophenyl ring in some of these compounds (Fig. 2A) encouraged us to synthesize ^{18}F -fluoroanalogs via copper-mediated late-stage radiofluorination (Fig. 2B). Since PET has shown high sensitivity and specificity to measure the expression of certain enzymes (e.g., esterases, glycosylases, hydrolases, and proteases (11)), we postulated that arginase imaging could be valuable for the detection and follow-up of arginase-related pathologies. As there are no radiotracers specifically targeting arginase reported in the literature, we developed, for the first time (to our knowledge), 2 ^{18}F -fluorinated quaternary α -amino acid–based arginase inhibitors derived from MARS compounds (the generic 2-amino-6-borono-2-(benzylpiperidin-4-yl)hexanoic acid compounds originally developed by Mars, Inc.).

MATERIALS AND METHODS

General Information

All substrates, reagents, and solvents were purchased from commercial suppliers and used as received without any purification unless otherwise noted. Air- and moisture-sensitive manipulations were performed using

Received Aug. 11, 2020; revision accepted Dec. 22, 2020.

For correspondence or reprints, contact Philip H. Elsinga (p.h.elsinga@umcg.nl).

Published online March 12, 2021.

© 2021 by the Society of Nuclear Medicine and Molecular Imaging.

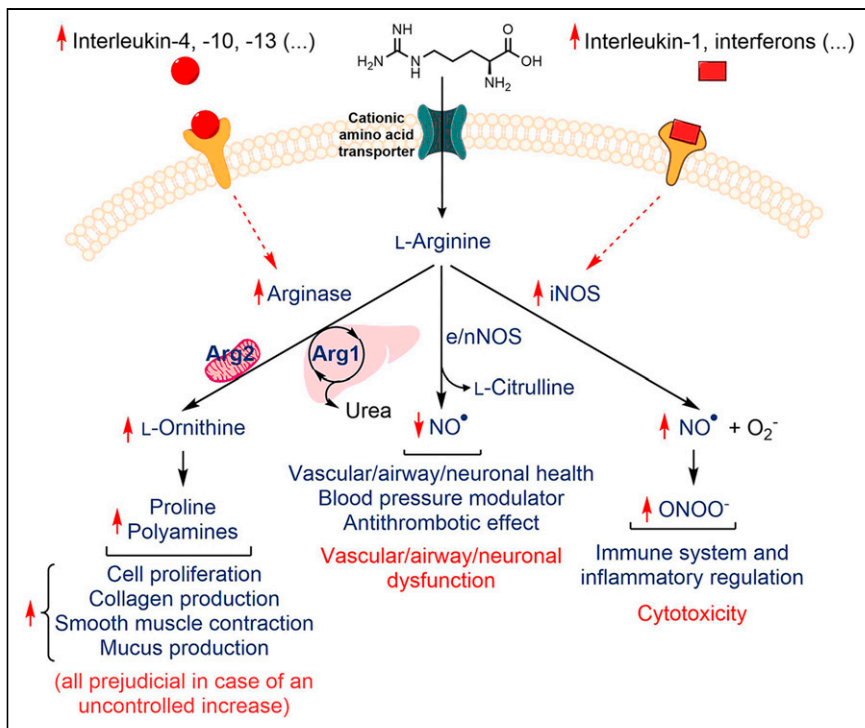


FIGURE 1. L-arginine metabolism outcomes associated with physiologic (blue) and pathophysiologic (red) expression of arginase and NOS. e/nNOS = endothelial/neuronal NOS; iNOS = inducible NOS.

oven-dried glassware under an atmosphere of argon or nitrogen. Air- and moisture-insensitive reactions were performed under ambient atmosphere and monitored by thin-layer chromatography (TLC) on silica gel or by liquid chromatography–mass spectrometry. Microwave reactions were performed in a Biotage Initiator Classic microwave. Thin-layer chromatography was performed on precoated silica gel 60 F₂₅₄ plates and visualized by fluorescence quenching under ultraviolet light. Flash chromatography purifications were performed using commercial normal-phase silica gel (40- to 63- μ m particle size). Concentration under

reduced pressure was performed by rotary evaporation at 23°C–40°C at an appropriate pressure. Final products were purified by Grace Reveleris X2 column chromatography using Grace Reveleris silica cartridges (12 or 40 g). Purified compounds were further dried under a vacuum (10^{-6} – 10^{-3} bar). Yields refer to purified and spectroscopically pure compounds.

Aqueous ^{18}F -fluoride used in this work was produced by the $^{18}\text{O}(p,n)^{18}\text{F}$ nuclear reaction in an IBA Cyclone 18/18 cyclotron. Manual radiolabeling was performed in radiochemistry fume hoods at negative air pressure with respect to the laboratory. Radiolabeled products were monitored and identified by radio-TLC and radio-high-performance liquid chromatography (HPLC).

High-resolution mass spectra were obtained using an electrospray ionization mass spectrometry system from Waters (Investigator Semiprep 15 Super Critical Fluid Chromatography) with a 3100 mass spectrometry–electrospray ionization detector using a solvent system of methanol (with ammonium hydroxide as an additive) and CO_2 on an ethyl pyridine 4.6×250 mm column or from the taken TLC silica gel plate using Advion plate express TLC–mass spectrometry. Semipreparative HPLC was performed on a Waters system using a 1525 binary HPLC pump, a 2489 ultraviolet-light/visible-light

detector, and a Berthold Technologies Flowstar LB 513 radio flow detector. Analysis of the synthesized radiotracers for assessment of final quality control was done using a Waters Acquity integrated system coupled to a Berthold Technologies Flowstar LB 513 radio flow detector. HPLC data were processed with Waters Empower 3 software. Radio-TLC printouts on phosphor imaging plates were scanned using a Perkin Elmer Packard Cyclone storage phosphor system, and the acquired data were analyzed with the OptiQuant 03.00 software. γ -counting was performed on a Perkin Elmer Wallac Wizard 1470, with an open energy window (15–1,000 keV) and 15 s of measuring time.

Nuclear MR spectra were recorded on a Bruker 500 spectrometer operating at 500 and 126 MHz for ^1H and ^{13}C acquisitions, respectively, in deuterated solvents. For ^1H nuclear MR, chemical shifts are reported in ppm, with the solvent residual peak as the internal standard, and coupling constants are reported in hertz. Chemical shifts for ^{13}C nuclear MR are reported in ppm relative to the solvent peak.

All animal procedures were performed following the European Union directives for animal experiments (86/609/CEE, 2003/65/CE, and 2010/63/EU), and the protocols used (AVD105002016395 for mouse work, and AVD10500201581 for guinea pig work) were previously approved by the Dutch National Committee on Animal Experiments and the Institutional Animal Care and Use Committee of the University of Groningen.

Messenger RNA Isolation and PCR Analysis

Total messenger RNA was isolated using Trizol RNA extraction (TRI Reagent Solution;

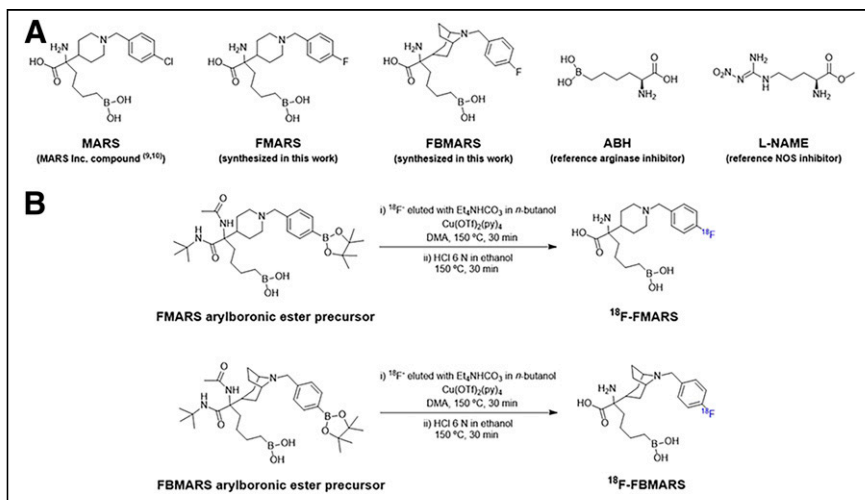


FIGURE 2. Molecules used in this work (A) and arylboronic ester–derived precursors with respective ^{18}F -fluorinated products (B). DMA = dimethylacetamide; MARS = 2-amino-6-borono-2-(1-(4-chlorobenzyl)piperidin-4-yl)hexanoic acid; FMARS = 2-amino-6-borono-2-(1-(4-fluorobenzyl)piperidin-4-yl)hexanoic acid; FBMARS = 2-amino-6-borono-2-(3-(4-fluorobenzyl)-3-azabicyclo[3.2.1]octan-8-yl)hexanoic acid; ABH = 2-(S)-amino-6-borono-hexanoic acid; L-NAME = N $^{\omega}$ -nitro-L-arginine methyl ester.

Applied Biosystems) according to the manufacturer's instructions. Complementary DNA was synthesized from equal amounts of RNA using the Reverse Transcriptase System (Promega) and the following protocol: 10 min at 25°C, 45 min at 42°C, and 5 min at 99°C. Reverse-transcription polymerase chain reaction was performed with SYBR Green (Roche Diagnostics) and the following protocol, including a final step to generate the melting curve: 2 min at 95°C, 10 min at 95°C, 45 × (30 s at 95°C, 30 s at 60°C, and 30 s at 72°C), 30 s at 95°C, 30 s at 55°C, and 30 s at 95°C. The reverse-transcription polymerase chain reaction was performed in an Eco system (Illumina). For analysis, LinReg software was used to calculate N_0 values, which were normalized to the N_0 of the housekeeping genes HPRT1 and GAPDH as an internal control. The primer sets used to analyze gene expression are shown in Table 1.

Surface Plasmon Resonance

Binding kinetics of the inhibitors were determined by surface plasmon resonance using a Biacore T200 (GE Healthcare). Arg1 was immobilized on a nickel-nitrilotriacetic acid sensor chip by nickel-mediated affinity capturing and amine coupling to a level of 4,000 or 6,000 resonance units using 60 µg/mL Arg1 in running buffer (50 mM Na₂HPO₄, pH 7.4, 150 mM KCl, and 0.01% polysorbate-20). The arginase inhibitors were diluted in the same running buffer and were injected in an increasing concentration range of 0.1, 0.316, 1.0, 3.16, and 10 µM. Single-cycle kinetics were used for measuring compound binding with a flow rate of 30 µL/min, an association time of 100 s per injection, and a dissociation time of 1,800 s. The compound response was subtracted with both the reference channel response and the blank injection. The Biacore evaluation software was used to fit the data to the Langmuir 1:1 binding model, with χ^2 values indicating minimal deviation between the fit and the experimental data. This minimal deviation was confirmed by determination of the reliability of the curve fits with standard Biacore checks. All combinations of the inhibitors and pH conditions were measured in at least 2 technical replicates to determine the kinetic association rate constant (k_a), dissociation rate constant (k_d), and equilibrium dissociation constant (K_D [binding affinity], or k_d/k_a). The target residence time (τ) was calculated from the k_d value as $1/k_d$.

PET Acquisition, Image Reconstruction, and Biologic Half-Life Calculation

The anesthetized animals were placed prone on a 38°C heating pad on the small-animal PET table to keep a constant body temperature. They were stretched out as much as possible to minimize organ superposition, and the tumor was positioned in the field of view. Subsequently, a 90-min emission scan was acquired with a Focus 220 rodent scanner (Siemens/Concorde). Between the injection time and the beginning of the scan, an average of 5 min passed. After completion of the PET scan, a 10-min transmission scan with a ⁵⁷Co point source was obtained for correction of scatter and attenuation of 511-keV photons by tissue.

For the small-animal PET image analysis, all emission scans were iteratively reconstructed (2-dimensional ordered-subsets expectation maximization, 4 iterations, 16 subsets) after being normalized and corrected for attenuation and radioactive decay. The list-mode data of the

emission scans were separated into 24 frames (6 × 10 s, 4 × 30 s, 2 × 60 s, 1 × 120 s, 1 × 180 s, 4 × 300 s, and 6 × 600 s). A 3-dimensional volume of interest was manually drawn by a single observer on the original dataset, delineating the desired area on the summed PET images (0–90 min) using the PMOD software package (version 3.9; PMOD Technologies LLC). These volumes of interest were used to create the corresponding time–activity curves and to calculate SUVs. A single exponential curve was fitted to the SUV time–activity curves (using values from 40 to 90 min) by an iterative nonlinear least-squares approach using Prism (version 6.01; GraphPad Software) for Microsoft Windows to calculate the biologic half-life of the tracer.

Synthesis and Characterization

Arginase and NOS inhibitors—2-(*S*)-amino-6-borono-hexanoic acid (ABH) and *N*^o-nitro-L-arginine methyl ester (L-NAME), respectively—were purchased (Merck) with purity of at least 98%. The MARS-derived standards (FMARS and FBMARS) and their respective arylboronic ester labeling precursors were synthesized by modifying a reported method (10). These compounds were used as a racemic mixture per the original reports (9,10) because the inhibitory potencies and pharmacokinetics of these α -carbon substituted ABH derivatives do not significantly differ from the optically active references (12,13). Synthesis details, characterization, instrumentation, and additional techniques are given in the supplemental materials (available at <http://jnm.snmjournals.org>).

Radiolabeling

The copper-mediated radiofluorination of the arylboronic ester derivatives was performed according to the reported alcohol-enhanced method (14) with our previous optimizations (15,16). Aqueous ¹⁸F-fluoride (5–10 GBq) was trapped on an anion-exchange cartridge (Chromafix 45-PS-HCO₃⁻), washed with 1 mL of *n*-butanol, dried with argon, and eluted with 0.4 mL of a tetraethylammonium bicarbonate solution in *n*-butanol (6.75 mg·mL⁻¹). To this ¹⁸F-fluoride solution was added 0.8 mL of dimethylacetamide containing the labeling precursor (4.5 µmol) and [Cu(OTf)₂(py)₄] (20 µmol). This mixture was stirred at 150°C for 30 min. Then, it was diluted in 40 mL of water and passed through an Oasis HLB solid-phase extraction cartridge to trap the ¹⁸F-fluorinated intermediate. After the cartridge was washed with water (10 mL), the ¹⁸F-fluorinated intermediate was recovered with 1.5 mL of ethanol, and 0.6 mL of HCl 6 N was added to remove the protecting groups. This mixture was left under stirring at 120°C for 30 min. The final product, ¹⁸F-FMARS or ¹⁸F-FBMARS, was isolated by HPLC. A Luna C18 5-µm 10 × 250 mm 100-Å column (Phenomenex) was used with a linear gradient from 100% to 80% aqueous trifluoroacetic acid (0.1%) in acetonitrile over 30 min (flow, 5 mL·min⁻¹). The collected peak was diluted in water, and the solvent was exchanged by trapping the product in an Oasis HLB cartridge and recovered with ethanol. The final solution was diluted with 0.02 M sodium acetate, pH 7.4 (maximum of 9% ethanol).

TABLE 1
Primer Sets Used to Analyze Gene Expression

Gene	Forward primer	Reverse primer
HPRT1	AAGCCAGACTTTGTGGATT	ACTGGCGATGTCAATAGGAC
GAPDH	CCAGCAAGAGCACAAAGAGGA	GAGATTCAGTGTGGTGGGGG
ARG1	GGAGACCACAGTTTGGCAAT	CCACTTGTGGTTGTCACTGG
ARG2	TGCATCCTTGAAGTGTGAGC	ACAAGCTGCTGCTTCCATT

Radiotracer Characterization

The radiotracers' purity was confirmed first by thin-layer chromatography, with TLC- Al_2O_3 developed in *n*-butanol: CH_3COOH : H_2O (12:3:5), and then by radio-HPLC using a Gemini C18 5- μm 150 \times 4.6 mm 110- \AA liquid chromatography column (Phenomenex) with a linear gradient from 100% to 50% of aqueous 0.1% trifluoroacetic acid in acetonitrile over 15 min (flow, 1.5 mL \cdot min $^{-1}$).

The lipophilicity (log *D*) was measured by dissolving each radiotracer in a 1:1 mixture of phosphate-buffered saline (PBS), pH 7.4, and *n*-octanol. This mixture was thoroughly stirred in a vortex mixer, centrifuged (3,000 rpm for 5 min), and left to rest. Triplicate samples from both phases were measured on a γ -counter. The reported log *D* value is the averaged ratio between the number of counts in the *n*-octanol and PBS layers.

For the in vitro stability assays, each radiotracer was left at room temperature and analyzed by radio-HPLC and radio-TLC at distinct time points up to 4 h. The stability was also evaluated by incubating the radiotracers with serum at 37°C, analyzing directly by radio-TLC, and analyzing after deproteinization with acetonitrile by radio-HPLC, at various time points up to 4 h.

Enzyme-Substrate Kinetics

ABH, MARS, FMARS, and FBMARS were evaluated for their ability to inhibit recombinant human Arg1 and Arg2. Half-maximal inhibitory concentration (IC₅₀) values were obtained with a colorimetric urea inhibition assay (8,12) performed in 96-well plates with a final volume of 60 μL per well for each reaction. Each arginase subtype (0.67 $\mu\text{g}/\text{mL}$) was preincubated with 5 concentrations (0.0167–167 μM) of the arginase inhibitors in PBS, for 30 min at 37°C. The reactions were started by adding 10 μL of L-arginine (120 mM) and were left to incubate for 1 h at 37°C. After quenching, the arginase activity was quantified with a Synergy ¹H Microplate Reader (Biotek) by spectrophotometric measurement (530 nm) of the urea produced, and the IC₅₀ values were calculated.

The enzyme-substrate binding kinetics of the arginase inhibitors were monitored in real time with a noninvasive label-free surface plasmon resonance ResidenceTimer assay developed by The Netherlands Translational Research Center in a BiaCore T200 (GE Healthcare) system (17). As no differences were seen between the IC₅₀ values for Arg1 and Arg2, and no significant changes in binding kinetics between isoforms are expected, only Arg1 was used for the kinetic assays. Arg1 was diluted in 50 mM Na_2HPO_4 , pH 7.4, 150 mM KCl, and 0.01% polysorbate-20, in a concentration of 60 $\mu\text{g}/\text{mL}$, and immobilized on a sensor chip. Five concentrations (0.1–10 μM) of the arginase inhibitors were injected into the system to measure binding.

Cell-Binding Assays

Mycoplasma-free arginase-expressing LNCaP and PC3 cell lines (18–22) obtained from the American Type Culture Collection (cultured in RPMI-1640 medium with 10% fetal bovine serum) were washed with PBS (37°C) and left for 30 min in PBS enriched with glucose (5.6 mM), MgCl_2 (0.49 mM), and CaCl_2 (0.68 mM), at 37°C (5% CO_2). For control assays, 25 μL of PBS were added to the wells. For competition assays, 25 μL of ABH, MARS, FMARS, or FBMARS in PBS (1 mM/well) were added. For the arginase/NOS specificity assays, 25 μL of L-NAME (1 mM/well) or 12.5 μL of L-NAME (1 mM/well) with 12.5 μL of MARS (1 mM/well) were added. After 30 min of preincubation (5% CO_2 , 37°C), 50 μL of the radiotracer (4 MBq \cdot mL $^{-1}$) were added to each well and left to incubate for another 30 min. Finally, the medium from all wells was removed and the cells were washed with cold PBS, trypsinized, detached, resuspended in medium (RPMI-1640 and 10% fetal bovine serum, 37°C), and transferred to test tubes. Each tube's radioactivity was determined in a γ -counter, and the viable cells were counted after trypan blue treatment.

Autoradiography Assays

A well-defined guinea pig model of asthma, showing increased expression of arginase in the lungs, has been developed by Meurs' group (23–25). Eight male Dunkin Hartley guinea pigs (Envigo) weighing approximately 250 g at the time of sensitization were used. The guinea pigs were housed conventionally in pairs, in ventilated cages in rooms maintained at a 12-h light/dark cycle, and were provided ad libitum access to food and water. The radiotracers were evaluated in 4- μm pulmonary cross-sections of this model. The lung sections of ovalbumin-sensitized guinea pigs challenged with saline (healthy control) or allergenic ovalbumin (asthmatic model) were washed by soaking in a solution of Trizma HCl (pH 7.4, 0.05 M; Sigma-Aldrich) with NaCl (120 mM), CaCl_2 (2 mM), and MgCl_2 (5 mM); left in this medium for 30 min; and then gently dried with an air stream. Each lung section was covered with 300 μL of a mixture of radiotracer (0.4 MBq) with or without an arginase inhibitor (1 mM) and left to incubate for 60 min. After incubation, all lung sections were washed with cold Trizma HCl (pH 7.4, 0.05 M) and ice-cold water and dried. These sections were then exposed to a phosphor imaging screen and quantified by a GE Healthcare Amersham Typhoon autoradiograph.

Animal Studies

Immune-deficient mice were inoculated with PC3 cells, which have higher tumorigenicity than LNCaP (26). Thirty-two immunocompromised male mice (6- to 8-wk-old BALB/c nude mice supplied by Envigo) were used. The animals were provided with sterilized chow and water ad libitum and were housed in individually ventilated cages equipped with a negative-pressure high-efficiency particulate air filtration system. During tumor inoculation or PET scanning, the mice were anesthetized with isoflurane (5% for induction and 2% for maintenance). Arginase gene expression in the PC3 cells was confirmed by real-time polymerase chain reaction (Supplemental Fig. 1). Inoculations were performed subcutaneously on each mouse's neck with a suspension of $2.0 \pm 1.0 \times 10^6$ PC3 cells in a 1:1 mixture of Matrigel and RPMI-1640 medium with 10% fetal bovine serum. The mice were scanned when tumors reached $0.45 \pm 0.15 \text{ cm}^3$. Tumor diameters were measured 1–3 times per week with a caliper, and tumor volume was calculated using the following formula: $V_{\text{tumor}} = ab^2/2$, where *a* and *b* represent tumor length and width, respectively. The mean body mass at the time of the radiotracer injection was $21.3 \pm 0.3 \text{ g}$. The radiotracer ($4.2 \pm 1.5 \text{ MBq}$; $92 \pm 56 \text{ pmol}$ estimated from the injected dose and molar activity) was administered through the penile vein with and without coinjection of arginase inhibitor (5 mM). After a dynamic 90-min emission scan and a 10-min transmission scan on a Focus 220 tomograph, the animals were euthanized, and urine and blood were collected to assess the radiotracer stability. Organs and tumors were harvested and weighed, and the radioactivity was determined to calculate the percentage injected dose per gram of tissue (%ID/g). For the small-animal PET image analysis, 3-dimensional volumes of interest delineating the desired area on the summed PET images (0–90 min) were drawn using PMOD software. For in vivo stability, urine and blood samples were collected approximately 2 h after injecting the radiotracer in BALB/c nude mice. Urine was directly analyzed by radio-HPLC and radio-TLC. Aliquots of the blood samples were directly analyzed by radio-TLC. The remaining blood was centrifuged (6,000 rpm for 3 min) to separate the plasma fraction. Plasma was directly analyzed by radio-TLC and, after deproteinization with acetonitrile, by radio-HPLC.

Statistics

Data are expressed as the mean \pm SD. All experiments were repeated at least 3 times independently. Unpaired 2-tailed *t* tests were used for statistical evaluations. A *P* value of less than 0.05 was considered statistically significant. Statistical analyses were performed using Prism.

TABLE 2
IC₅₀ and Enzyme-Substrate Kinetics of Arginase Inhibitors

Substrate	IC ₅₀ (pH 7.4)		Arg1-substrate kinetics (pH 7.4)				
	Arg1 (μM)	Arg2 (μM)	K _D (M)	k _d [*] (s ⁻¹)	k _a [†] (M ⁻¹ ·s ⁻¹)	t _{1/2} [‡] (s)	τ (s)
ABH	1.4	1.1	4.38 × 10 ⁻⁷	1.10 × 10 ⁻²	2.51 × 10 ⁴	63	91
MARS	0.9	0.7	1.48 × 10 ⁻⁷	3.90 × 10 ⁻⁴	2.64 × 10 ³	1,775	2,561
FMARS	1.1	0.4	3.16 × 10 ⁻⁷	8.90 × 10 ⁻⁴	2.82 × 10 ³	779	1,123
FBMARS	0.04	0.05	2.28 × 10 ⁻⁷	3.47 × 10 ⁻³	1.52 × 10 ⁴	200	288

*Fraction of arginase-substrate complexes dissociating per second.
†Arginase-substrate complexes formed per second in 1 M solution.
‡Dissociative half-life (ln[2]•τ).

RESULTS

Compound Characterization and Radiolabeling

The synthesis of MARS, FMARS, and FBMARS yielded 16% ± 3% for all 3 compounds. Further evaluation of these arginase inhibitors confirmed their similar potency to inhibit both enzyme isoforms indistinctly (IC₅₀, 0.04–1.4 μM; Table 2). The K_D values for all arginase inhibitors to Arg1 were similar (148–438 nM) and in agreement with the literature (27). The results are shown in Table 2 and Supplemental Figure 2.

¹⁸F-FMARS and ¹⁸F-FBMARS were radiosynthesized from the respective arylboronic ester precursors, purified, and reformulated into injectable solutions in approximately 105 min. A final radiochemical yield of 4% ± 1% (decay-corrected) was achieved, with a molar activity of 53 ± 19 GBq·μmol⁻¹. Both radiotracers showed a radiochemical purity of more than 95%, either at the end of synthesis (Supplemental Fig. 3) or during the stability studies in solution or serum up to 4 h (Supplemental Figs. 4–7). A log D of -0.7 ± 0.1 and -1.0 ± 0.1 (at pH 7.4) was experimentally calculated for ¹⁸F-FMARS and ¹⁸F-FBMARS, respectively.

Cell-Binding Assays

Both radiotracers showed cellular uptake associated with arginase expression, as this binding effect was reduced after pretreatment with competitive inhibitors (Fig. 3). The overall blocking efficiency in both cell lines was 47% ± 8% for MARS, FMARS, and FBMARS, whereas for ABH it was 22% ± 6%. Cells were also pretreated with the selective NOS inhibitor L-NAME to confirm specificity for arginase. When PC3 cells were incubated with L-NAME and an arginase inhibitor, the tracer's uptake decreased 50% ± 5% (P = 0.0002).

Asthmatic Lung Model

Incubation of ¹⁸F-FMARS and ¹⁸F-FBMARS with control lung sections showed residual binding, whereas an approximately 10-fold increase was seen in sections from allergen-challenged animals (Fig. 4; Supplemental Fig. 8), correlating to the well-characterized overexpression of arginase in this asthmatic model (24,25). The blocking effect in asthmatic lung sections treated with arginase inhibitors (maximum, 60%; P = 0.02) reiterated the radiotracers' specificity toward arginase.

¹⁸F-FMARS/¹⁸F-FBMARS Biodistribution

After confirmation of arginase gene expression in the PC3 cells, immunocompromised mice were inoculated with this cell line

(Supplemental Fig. 9). A pilot screening was performed with ¹⁸F-FBMARS in the PC3 xenograft model to evaluate which arginase inhibitor (ABH or MARS) shows superior in vivo inhibitory effect. By significantly reducing tumor uptake (Supplemental Fig. 10), ABH was selected to evaluate the in vivo arginase specificity of both radiotracers.

Biodistribution studies with ¹⁸F-FMARS and ¹⁸F-FBMARS after small-animal PET scans confirmed arginase-mediated uptake (Fig. 5; Supplemental Table 1). A generalized decline in uptake in ABH coinjection experiments was also seen because of arginase ubiquity (28). Relatively high uptake in the kidneys and moderate uptake in the liver indicate a preference for urinary excretion but can also be related to high expression of arginase in these organs, since uptake was reduced by ABH. A prominent blocking effect in endocrine and intestinal tissues was observed, as these are known to highly express Arg2 (29). The %ID/g for harvested tumors showed a significant reduction in ¹⁸F-FBMARS uptake (70% ± 19%, P < 0.0001) after ABH coinjection. Combined with a tumor-to-organ ratio

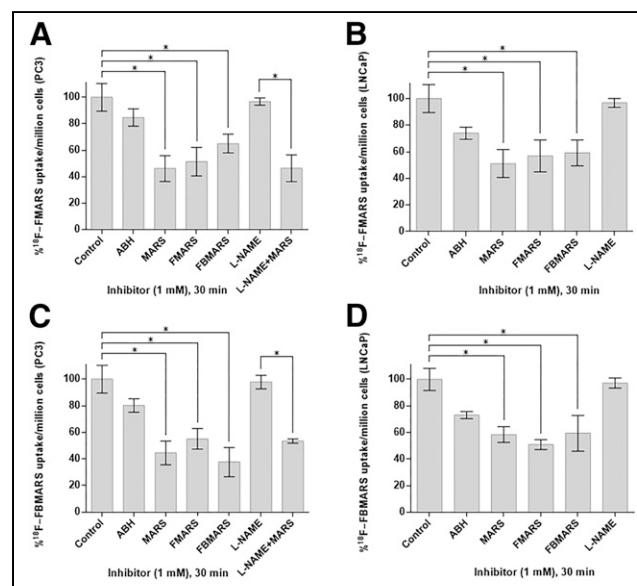


FIGURE 3. ¹⁸F-FMARS (A and B) and ¹⁸F-FBMARS (C and D) uptake in PC3 and LNCaP cells without (control) and with competitive inhibition (n ≥ 3, *P < 0.05). Data are expressed as percentage of cell-associated radioactivity per 1 million cells.

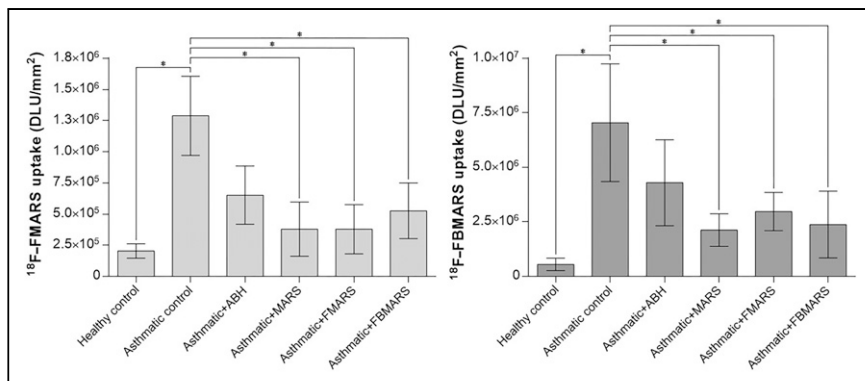


FIGURE 4. ^{18}F -FMARS and ^{18}F -FBMARS uptake in digital luminescence units (DLU) per mm^2 in saline-challenged (healthy) and allergen-challenged (asthmatic) guinea pig lung sections without (control) and with competitive arginase inhibition ($n = 4$, $^*P < 0.05$).

generally higher than 2 (Supplemental Fig. 11), this finding highlights the particular potential of ^{18}F -FBMARS to differentiate arginase-overexpressing tumors from nontarget tissues. Radiometabolites and ^{18}F -defluorination products were not detected in plasma and urine analysis (Supplemental Figs. 12–15).

Small-Animal PET Imaging

A 90-min dynamic PET study was performed on mice bearing PC3 tumors to evaluate the potential of ^{18}F -FMARS and ^{18}F -FBMARS to map arginase expression in vivo (Fig. 6). A maximum SUV of 3.1 ± 0.7 in the tumor and a signal reduction of up to 60% ($P < 0.01$) when ABH was coinjected confirmed an arginase-mediated uptake. Furthermore, because of the generalized arginase expression, a decrease in tracer uptake was seen after treatment with arginase inhibitor, especially in the salivary and Harderian glands, which are known to highly express arginase (30).

Time-activity curves indicated rapid blood clearance for both radiotracers (Fig. 7), as maximum uptake in the heart was reached in less than 5 min after injection, then decreasing exponentially with a biologic half-life of 7.3 ± 0.6 min. Accumulation of ^{18}F -FMARS and ^{18}F -FBMARS in PC3 tumors was clearly visualized, peaking at approximately 40 min after injection and showing a subsequent slow decrease (biologic half-life, ~ 105 min). When the

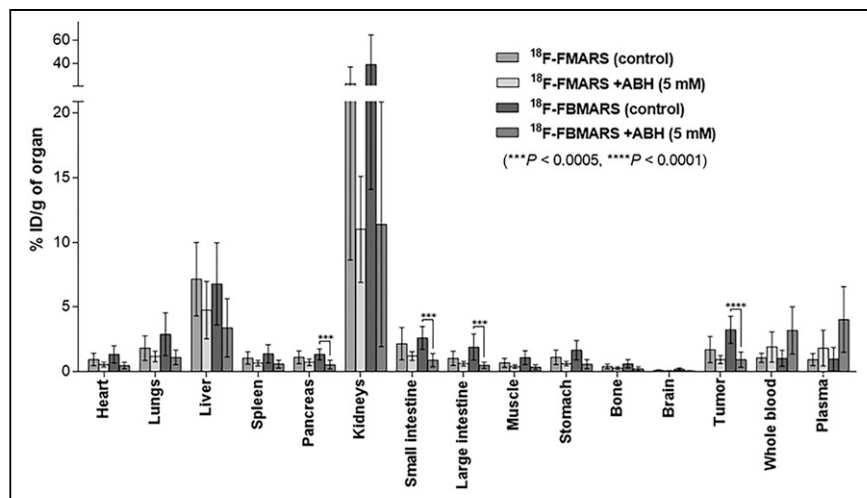


FIGURE 5. Biodistribution of ^{18}F -FMARS ($n = 7$) and ^{18}F -FBMARS ($n = 9$), with and without ABH coinjection, approximately 2 h after injection in PC3 xenograft mice.

radiotracers were coinjected with ABH, accumulation in the PC3 tumors was lower, reaching its maximum at 17.5 min after injection and then decreasing exponentially more rapidly than in controls (biologic half-life, 67.7 ± 8.1 min). However, the difference in tumor uptake between control and ABH-treated groups did not become statistically significant until approximately 33 min after the ^{18}F -FBMARS injection.

DISCUSSION

The substitution of a chlorophenyl (MARS) by a fluorophenyl group (FMARS) did not affect the affinity or inhibitory potency to arginase but reduced the residence time on the active site. The longer residence time of MARS indicates a better potential to treat arginase-overexpressing pathologies due to a prolonged pharmacodynamic effect. Nevertheless, reversible inhibitors such as α -carbon substituted ABH derivatives derivatives (7) have a high k_a , favoring PET imaging. Their radiolabeled analogs will rapidly accumulate in sites with high expression of the target enzyme and more effectively clear from nontarget regions (11). The rapid clearance of these arginase inhibitors (31) may result in less background signal.

To increase k_a , the piperidine moiety of FMARS was replaced by a tropane group (FBMARS) (10). This modification locks the molecule in a conformation that benefits interaction with the amino acid residues of the active site (10), leading to a 10-fold increase in arginase inhibitory activity and enzyme-inhibitor complex formation rate. Thus, to evaluate arginase mapping potential, ^{18}F -fluorinated analogs (^{18}F -FMARS and ^{18}F -FBMARS) were successfully synthesized with molar activity comparable to other ^{18}F -labeled tracers used in the clinic (32).

Preliminary assays in arginase-overexpressing prostate cancer cells showed specific binding of both radiotracers to arginase, as the cellular uptake decreased after pretreatment with arginase inhibitors. The specificity of the radiotracers to arginase over NOS was confirmed by the inefficiency of the selective NOS inhibitor L-NAME to affect ^{18}F -FMARS and ^{18}F -FBMARS uptake. Nonspecific residual binding was visible after pretreatment with arginase inhibitors, as was expected since boronic acids are known to react with carbohydrates in the cell membrane (33). This interaction is common to all classic boronic acid inhibitors at physiologic pH.

Competitive binding assays with results comparable to those obtained in cells were seen in guinea pig lung sections. The 10-fold increase seen in the binding of both radiotracers to allergen-challenged lungs was related to the overexpression of arginase in the asthmatic airways (24,25,34). ^{18}F -FMARS and ^{18}F -FBMARS uptake was reduced after pretreatment of the asthmatic lung sections with arginase inhibitors. An increased arginase expression is also present in the lungs of asthmatic patients and associated with higher severity

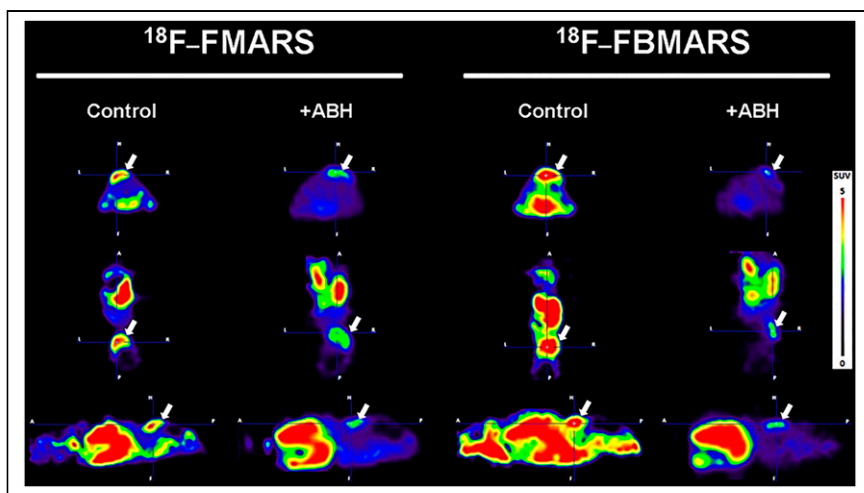


FIGURE 6. Representative maximum-intensity-projection small-animal PET images (40–90 min) centered on PC3 tumor (arrows; axial, coronal, and sagittal views from top to bottom) of mice injected with ^{18}F -FMARS or ^{18}F -FBMARS, without (control) and with coinjection of ABH (5 mM).

(35,36). Arginase inhibitors are therefore considered a potential approach to treating asthma (6). FBMARS may be considered a candidate drug, whereas ^{18}F -FMARS or ^{18}F -FBMARS may become imaging tools for patient selection or treatment follow-up.

Despite showing weaker inhibition *in vitro*, ABH demonstrated a more efficient blocking effect than MARS *in vivo*. Since ABH has a K_D , IC_{50} , and hydrophilicity similar to the MARS compounds (10), its lower *in vitro* effect may be explained by a much shorter τ . *In vitro* binding assays involve the abrupt washout of the unbound substrate, a procedure known to underestimate the efficiency of reversible ligands with a brief τ when compared with the *in vivo* assessments (37). This discrepancy in blocking efficiency may also be explained by differences in bioavailability, membrane penetration capacity, or clearance rate between ABH and MARS or by potential alterations in the expression of cationic amino acid transporters or other endogenous processes between the *in vitro* and *in vivo* models used. These observations suggest that novel arginase inhibitors should be evaluated in complex biologic systems after being screened with purified arginase or in controlled cellular microenvironments (12,31). Thus, real-time assessment of the pharmacokinetics and therapeutic efficacy of arginase inhibitors within living subjects may be facilitated using PET.

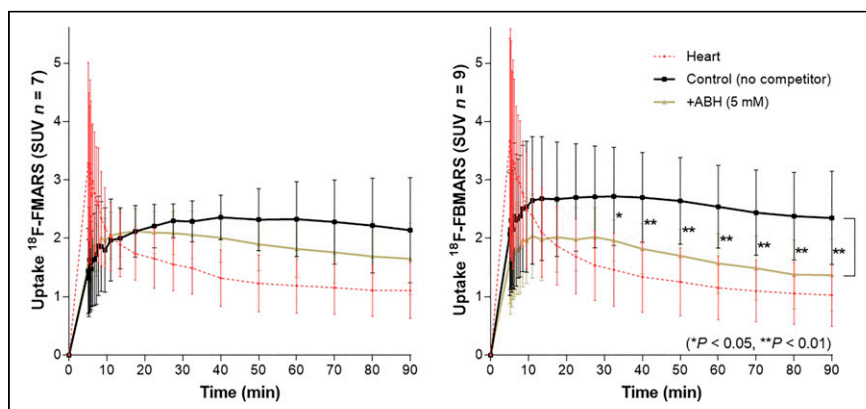


FIGURE 7. Time-activity curves of ^{18}F -FMARS ($n = 7$) and ^{18}F -FBMARS ($n = 9$). SUVs are in PC3 xenograft mice without (control) and with ABH coinjection.

The potential of ^{18}F -FMARS and ^{18}F -FBMARS to map arginase expression was evaluated in PC3 xenograft mice. Tumor-to-organ ratios were higher and uptake differences between control and blocked animals more significant for ^{18}F -FBMARS than for ^{18}F -FMARS. *In vivo* assays reaffirmed the radiotracers' specificity since the uptake in the arginase-expressing tumors was clearly reduced with ABH coinjection. Global suppression of radiotracer uptake by ABH was also noticed because of the widespread ubiquity of arginase (28). ^{18}F -FBMARS produced a more intense signal than ^{18}F -FMARS, as was also seen in pulmonary autoradiography. The statistically significant difference between ^{18}F -FBMARS tumor uptake with and without inhibitor 40 min after injection makes this radiotracer the best choice for arginase mapping.

Nevertheless, none of the radiotracers showed isozyme selectivity, and molecules with such capacity remain challenging to attain because of the active sites' structural similarity (38). Poor selectivity for Arg2 causes undesirable radiotracer uptake in the liver, with consequences for dosimetry. Hepatic radiation dose may be reduced by previously administering N^{ω} -hydroxy-L-arginine, known to be up to 18 times more potent in inhibiting arginase activity in the liver than in nonhepatic tissues (39).

Because the development of therapeutically potent arginase inhibitors is a very active topic, ^{18}F -FBMARS may serve as a potential PET tracer to aid the pharmaceutical industry by, for example, enabling real-time *in vivo* arginase mapping studies to prove the target occupancy and pharmacodynamics of novel molecules. A possible limitation of our tracers may be the poor discrimination between inflammatory and carcinogenic tissues, leading to false-positives. However, the tracers may be relevant for immune therapy, as arginase is involved in the regulation of tumor-induced immune tolerance and arginase inhibition promotes the formation of an inflammatory microenvironment favoring a cancer-specific immune response (40). Therefore, the use of arginase inhibitors has been proposed for the treatment of certain tumors. ^{18}F -FBMARS may be used to select patients who could benefit the most from immunotherapy treatments.

CONCLUSION

We report the development of ^{18}F -fluorinated arginase inhibitors for PET imaging of arginase expression. These inhibitors showed a high affinity toward arginase. ^{18}F -FBMARS showed the highest arginase-mediated uptake in PC3 xenografts. These results encourage further exploration of the suitability of using ^{18}F -FBMARS to select patients who can benefit from treatments with arginase inhibitors.

DISCLOSURE

This work was supported by the Dutch Open Technologiëprogramma from NWO Toegepaste en Technische Wetenschappen

(project 13547). No other potential conflict of interest relevant to this article was reported.

ACKNOWLEDGMENTS

We thank Douwe F. Samplonius (Faculty of Medical Sciences, University of Groningen) for providing cell lines. We also thank I. Sophie T. Bos (Faculty of Science and Engineering, University of Groningen) for the guinea pig lung sections.

KEY POINTS

QUESTION: Are arginase inhibitors suitable PET tracers for mapping arginase expression?

PERTINENT FINDINGS: The synthesis and evaluation of radiolabeled arginase inhibitors are reported. The novel ^{18}F -fluorinated arginase inhibitors showed high affinity and arginase-specific *in vivo* binding and, thus, the potential to map increased arginase expression related to inflammatory and tumorigenic processes.

IMPLICATIONS FOR PATIENT CARE: Radiofluorinated arginase inhibitors may be explored as PET tracers to select patients who can benefit from treatments with arginase inhibitors.

REFERENCES

1. Dzik JM. Evolutionary roots of arginase expression and regulation. *Front Immunol*. 2014;5:544.
2. Caldwell RW, Rodriguez PC, Toque HA, et al. Arginase: a multifaceted enzyme important in health and disease. *Physiol Rev*. 2018;98:641–665.
3. Moretto J, Girard C, Demougeot C. The role of arginase in aging: a systematic review. *Exp Gerontol*. 2019;116:54–73.
4. Pham T-N, Liagre B, Girard-Thernier C, et al. Research of novel anticancer agents targeting arginase inhibition. *Drug Discov Today*. 2018;23:871–878.
5. S Clemente G, van Waarde A, Antunes IF, et al. Arginase as a potential biomarker of disease progression: a molecular imaging perspective. *Int J Mol Sci*. 2020;21:5291.
6. Meurs H, Zaagsma J, Maarsingh H, van Duin M. Recent patents in allergy/immunology: use of arginase inhibitors in the treatment of asthma and allergic rhinitis. *Allergy*. 2019;74:1206–1208.
7. Pudlo M, Demougeot C, Girard-Thernier C. Arginase inhibitors: a rational approach over one century. *Med Res Rev*. 2017;37:475–513.
8. van den Berg MP, Kurhade SH, Maarsingh H, et al. Pharmacological screening identifies SHK242 and SHK277 as novel arginase inhibitors with efficacy against allergen-induced airway narrowing *in vitro* and *in vivo*. *J Pharmacol Exp Ther*. 2020;374:62–73.
9. Van Zandt M, Golebiowski A, Ji MK, Whitehouse D, Ryder T, Beckett P, inventors; Mars, Inc., assignee. Inhibitors of arginase and their therapeutic applications. U.S. patent application WO/2011/133653. October 27, 2011.
10. Golebiowski A, Whitehouse D, Beckett RP, et al. Synthesis of quaternary α -amino acid-based arginase inhibitors via the Ugi reaction. *Bioorg Med Chem Lett*. 2013; 23:4837–4841.
11. Rempel BP, Price EW, Phenix CP. Molecular imaging of hydrolytic enzymes using PET and SPECT. *Mol Imaging*. 2017;16:1536012117717852.
12. Golebiowski A, Beckett RP, Van Zandt M, et al. 2-substituted-2-amino-6-boronohexanoic acids as arginase inhibitors. *Bioorg Med Chem Lett*. 2013;23:2027–2030.
13. Blaszczyk R, Brzezinska J, Dymek B, et al. Discovery and pharmacokinetics of sulfamides and guanidines as potent human arginase I inhibitors. *ACS Med Chem Lett*. 2020;11:433–438.
14. Zischler J, Kolks N, Modemann D, et al. Alcohol-enhanced Cu-mediated radiofluorination. *Chemistry*. 2017;23:3251–3256.
15. Zarganes-Tzitzikas T, Clemente GS, Elsinga PH, Dömling A. MCR scaffolds get hotter with ^{18}F -labeling. *Molecules*. 2019;24:1327.
16. Clemente GS, Zarganes-Tzitzikas T, Dömling A, Elsinga PH. Late-stage copper-catalyzed radiofluorination of an arylboronic ester derivative of atorvastatin. *Molecules*. 2019;24:4210.
17. Grobben Y, Uitdehaag JCM, Willemsen-Seegers N, et al. Structural insights into human arginase-I pH dependence and its inhibition by the small molecule inhibitor CB-1158. *J Struct Biol X*. 2019;4:100014.
18. Cederbaum SD, Yu H, Grody WW, et al. Arginases I and II: do their functions overlap? *Mol Genet Metab*. 2004;81(suppl):S38–S44.
19. Sigala S, Bodei S, Missale C, et al. Gene expression profile of prostate cancer cell lines: effect of nerve growth factor treatment. *Mol Cell Endocrinol*. 2008;284:11–20.
20. Mumenthaler SM, Yu H, Tze S, et al. Expression of arginase II in prostate cancer. *Int J Oncol*. 2008;32:357–365.
21. Hsueh EC, Knebel SM, Lo W-H, et al. Deprivation of arginine by recombinant human arginase in prostate cancer cells. *J Hematol Oncol*. 2012;5:17.
22. Ino Y, Yamazaki-Itoh R, Oguro S, et al. Arginase II expressed in cancer-associated fibroblasts indicates tissue hypoxia and predicts poor outcome in patients with pancreatic cancer. *PLoS One*. 2013;8:e55146.
23. Meurs H, Santing RE, Remie R, et al. A guinea pig model of acute and chronic asthma using permanently instrumented and unrestrained animals. *Nat Protoc*. 2006;1:840–847.
24. Maarsingh H, Zaagsma J, Meurs H. Arginase: a key enzyme in the pathophysiology of allergic asthma opening novel therapeutic perspectives. *Br J Pharmacol*. 2009;158: 652–664.
25. Maarsingh H, Dekkers BGJ, Zuidhof AB, et al. Increased arginase activity contributes to airway remodelling in chronic allergic asthma. *Eur Respir J*. 2011;38:318–328.
26. Wu X, Gong S, Roy-Burman P, et al. Current mouse and cell models in prostate cancer research. *Endocr Relat Cancer*. 2013;20:R155–R170.
27. Di Costanzo L, Ilies M, Thorn KJ, Christianson DW. Inhibition of human arginase I by substrate and product analogues. *Arch Biochem Biophys*. 2010;496:101–108.
28. Morris SM, Bhamidipati D, Kepka-Lenhart D. Human type II arginase: sequence analysis and tissue-specific expression. *Gene*. 1997;193:157–161.
29. The Human Protein Atlas website. <http://www.proteinatlas.org>. Accessed March 29, 2021.
30. Yasuda N, Moriwaki K, Furuyama S. Distribution and properties of arginase in the salivary glands of four species of laboratory mammals. *J Comp Physiol [B]*. 2004; 174:237–242.
31. Abdelkawy KS, Lack K, Elbarbry F. Pharmacokinetics and pharmacodynamics of promising arginase inhibitors. *Eur J Drug Metab Pharmacokinet*. 2017;42:355–370.
32. Huisman MC, Niemeijer A-L, Windhorst B, et al. Quantification of PD-L1 expression with ^{18}F -BMS-986192 PET/CT in patients with advanced stage non-small-cell lung cancer. *J Nucl Med*. 2020;61:1455–1460.
33. Achilli C, Ciana A, Fagnoni M, et al. Susceptibility to hydrolysis of phenylboronic pinacol esters at physiological pH. *Cent Eur J Chem*. 2013;11:137–139.
34. Pera T, Zuidhof AB, Smit M, et al. Arginase inhibition prevents inflammation and remodeling in a guinea pig model of chronic obstructive pulmonary disease. *J Pharmacol Exp Ther*. 2014;349:229–238.
35. Lara A, Khatri SB, Wang Z, et al. Alterations of the arginine metabolome in asthma. *Am J Respir Crit Care Med*. 2008;178:673–681.
36. Xu W, Comhair SAA, Janocha AJ, et al. Arginine metabolic endotypes related to asthma severity. *PLoS One*. 2017;12:e0183066.
37. Vauquelin G. Rebinding: or why drugs may act longer *in vivo* than expected from their *in vitro* target residence time. *Expert Opin Drug Discov*. 2010;5:927–941.
38. Ash DE. Structure and function of arginases. *J Nutr*. 2004;134(suppl):2760S–2764S.
39. Baggio R, Emig FA, Christianson DW, et al. Biochemical and functional profile of a newly developed potent and isozyme-selective arginase inhibitor. *J Pharmacol Exp Ther*. 1999;290:1409–1416.
40. Timosenko E, Hadjinicolaou AV, Cerundolo V. Modulation of cancer-specific immune responses by amino acid degrading enzymes. *Immunotherapy*. 2017;9: 83–97.